Radio Frequency Measurements of Energetic-Particle-Driven Emission using the Ion Cyclotron Emission Diagnostic on the DIII-D tokamak[a)]

K.E. Thome,[1, b)] D.C. Pace,[2] R.I. Pinsker,[2] O. Meneghini,[2] C.A. del Castillo,[3] and Y. Zhu[4]
[1)] *Oak Ridge Associated Universities PO Box 117, Oak Ridge, TN 37831, United States of America*
[2)] *General Atomics, PO Box 85608, San Diego, CA 92186-5608, United States of America*
[3)] *Stony Brook University, Stony Brook, NY, USA*
[4)] *University of California Irvine, Irvine, CA 92697, United States of America*

(Dated: Presented 19 April 2018)

The Ion Cyclotron Emission (ICE) diagnostic on the DIII-D tokamak consists of two outboard midplane systems. In the first system, straps of an ion cyclotron range of frequencies antenna are configured as receiving antennas. For the second system, dedicated magnetic probes incorporated into the outer wall of carbon tiles have recently been restored. These systems collected a large set of radio frequency measurements in the 2015-2018 experimental campaigns by digitizing signals at 200 MSamples/sec for ∼5 seconds per discharge. Each shot typically yields 32 GB of data; techniques for successful handling and analysis of this challengingly large dataset are discussed. The raw voltage fluctuations (<0.2 V and <1 mW) are analyzed in frequency space via fast Fourier transforms. Signals can be analyzed between 1–200 MHz with appropriate filtering and aliasing; this frequency range is limited by DC breaks used to provide 5 kV DC isolation. Three types of high-frequency emission driven by energetic particles have so far been observed using this diagnostic: Compressional Alfvén Eigenmodes with f < 10 MHz, ICE from 5–100 MHz, and whistler waves with f > 100 MHz. ICE occurs at harmonics of the ion cyclotron frequency, enabling the frequency to be mapped to lab space via EFIT equilibrium reconstructions.

PACS numbers: 52.70.Gw, 52.55.Fa, 52.35.Qz, 52.35.Hr
Keywords: fast magnetic measurements, high-frequency energetic particle emission, ion cyclotron emission

I. INTRODUCTION

Diagnosis of the fast-ion population in burning plasmas is critical to optimizing reactor performance. Superthermal ions, including fusion alphas, injected beam ions, and rf-accelerated ions, are responsible for heating the thermal ions to thermonuclear fusion temperatures. Thus an understanding of the confinement and dynamics of these energetic ions is critical to mitigating radial fast-ion transport and fast-ion losses, particularly first wall damage from fast ions[1]. In modern-day tokamaks, energetic ions are often diagnosed using cameras and probes, which will not survive sufficiently long in a reactor neutron radiation environment[2].

An alternative diagnostic tool of fast ions in a burning plasma is a simple magnetic pick-up loop. Many modern fusion experiments have observed emission in the Ion Cyclotron Range of Frequencies (ICRF) excited by energetic ions with such a diagnostic[3]. This high-frequency emission is predicted to occur in ITER, driven by the various fast ions present[4]. A magnetic pickup loop on ITER would be compatible with its D-T radiation environment and would serve as a passive, non-invasive diagnostic that could also provide information about the reactor fast-ion population.

Recently on DIII-D[5], the Ion Cyclotron Emission (ICE) diagnostic has been reestablished and significantly upgraded to measure this ICRF emission[6]. Energetic ions, primarily ions generated by the neutral beams, have been observed to drive two categories of signals on DIII-D. The first is referred to simply as Ion Cyclotron Emission (ICE), which this version of this diagnostic was established to measure. This emission with $f \geq f_{ci}$ where f_{ci} is the ion cyclotron frequency has been studied since the late 1980s on DIII-D[7–9] and initial observations of this emission measured with the upgraded diagnostic were presented in 2016[6]. ICE is sharply peaked at integer harmonics of f_{ci}. It has been detected on many past and present-day tokamaks: first on TFR[10], then in the D-T machines TFTR[11] and JET[12], and more recently on ASDEX-U[13], JT-60U[14], KSTAR[15], and even on the stellarator LHD[16]. The other kind of energetic-ion-driven emission, characterized by $f < f_{ci}$, is the Compressional Alfvén Eigenmode (CAE), first documented on DIII-D in 2006[17]. CAEs are observed regularly on the spherical tokamaks NSTX[18] and MAST[19], and the CAEs have been found to enhance energy transport on these devices[20]. Another type of ICRF energetic-particle-driven emission, whistler waves with $f >> f_{ci}$, has recently been observed by this diagnostic on DIII-D. This is the first observation of whistler waves in a tokamak[21], which are excited by multi-MeV runaway electrons present in low-density $n_e \sim 10^{19}$ m^{-3}

[a)] Contributed paper published as part of the Proceedings of the 22nd Topical Conference on High-Temperature Plasma Diagnostics, San Diego, California, April, 2018.
[b)] Electronic mail: thomek@fusion.gat.com

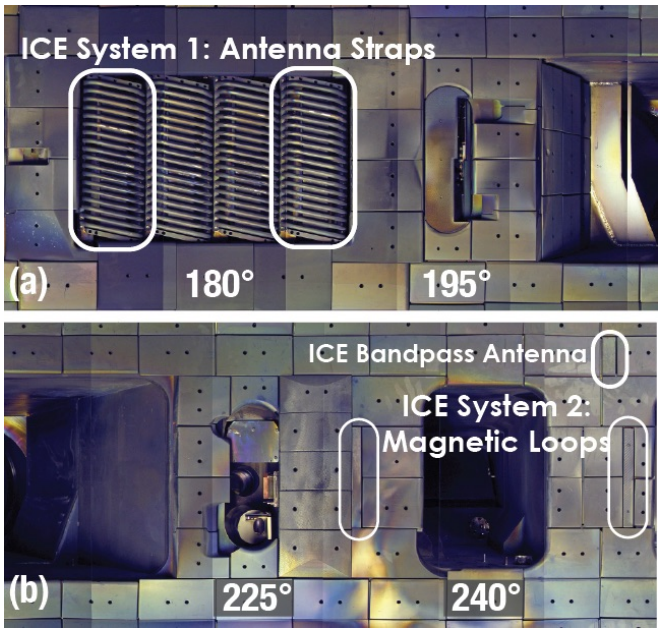

FIG. 1. ICE diagnostic on DIII-D. (a) System 1: antenna straps (b) System 2: ICE magnetic probes and bandpass ICE with used antenna circled.

plasmas.

In this paper, we describe the DIII-D ICE diagnostic (section II) and its data analysis and initial results (section III).

II. DIAGNOSTICS SETUP

At DIII-D, diagnostic locations are identified by their toroidal angle; this applies to all subsequent angle measurements. The ICE diagnostic consists of two outboard midplane systems as shown in Fig. 1. The two outer straps of the 180° ICRF antenna (System 1 in Fig. 1(a)) were instrumented for this diagnostic in 2015. These two straps are 10° toroidally apart. The second system of dedicated magnetic probes incorporated into the carbon tiles (System 2 in Fig. 1(b)) was restored in 2017. This system was previously used for density interferometer and ion species reflectometer measurements[22,23]. System 2 contains two antenna probes located behind the plasma facing portion of the carbon tiles with a spacing of 15° toroidally, separated by approximately 50° from System 1. Another tile antenna probe, separated poloidally from the other probes, is also used for low and high bandpass measurements and was previously described in Heidbrink *et al.*[9] These tile antenna probes (System 2 and bandpass) each consist of only a single loop to maintain their low inductance and thus high frequency response. Great care is taken to avoid contact between the tile antenna loops and neighboring tiles.

A block diagram of the electronic components of these two systems is shown in Fig. 2. The outputs of the antenna straps (System 1) connect to a plastic enclosure via RG58 cable. Within the vacuum vessel, the antenna probes (System 2) connect to a SMA feedthrough via a semi-rigid, bakeable vacuum-compatible coaxial cable

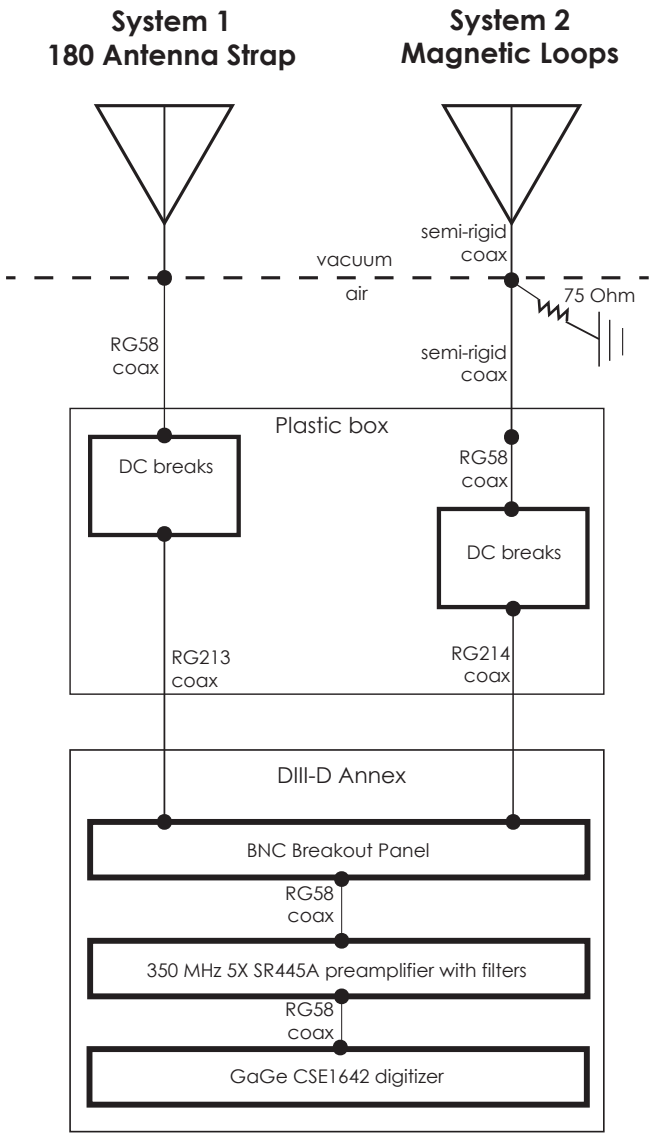

FIG. 2. Block diagram of ICE diagnostic.

with a characteristic impedance of about 30 Ω. On the air side of the feedthrough, the SMA connectors are connected in parallel to a 75 Ω impedance-matching resistor and 50 Ω semi-rigid cables. Another semi-rigid coaxial cable transmits the signal to a BNC breakout panel within the plastic box. Inside this box, both ICE systems then connect to safety breaks, designed to provide 5 kV DC isolation for both inner and outer conductors. All three systems use slightly different DC break designs, but all originate from the RF program. The signal is transmitted to the electronic annex via RG213 (System 1) or RG214 (System 2) cables that have an electrical length of at least 75 m. In the annex, the cables terminate on a BNC breakout panel. Within the DIII-D annex, RG58 cables are used. First, the signals are amplified by 5× (14 dB) with a 350 MHz SR445A preamplifier, then they are digitized using a 200 MHz GaGe CSE1642 digitizer. Typically, the signals are anti-aliased using a MiniCircuits BLP-100+ low-pass filter before the amplifier, providing data below the 100 MHz Nyquist frequency. However, in

the case of whistler waves, the data is either intentionally aliased using a MiniCircuits BHP-100+ high-pass filter to acquire signals in the 100-200 MHz band or the data is mixed down to the 0-100 MHz band.

The frequency response of these systems is limited by the DC breaks. These breaks have an approximately flat electrical response from 1 MHz to $\sim$ 120 MHz, with a 3 dB point at $\sim$ 150 MHz. Data up to 200 MHz has been recorded. The frequency response of these breaks includes a few-MHz-wide resonance between 40 and 60 MHz, an artifact of the old design. Future designs of the DC breaks will improve the frequency response by removing this resonance and increasing the frequency bandwidth to higher frequencies, thus facilitating further study of the whistler waves.

The magnetic fluctuation data is stored in MDSplus in 80 ms segments for up to 5.04 s of data. This amounts to 8 GB per channel per shot of data storage; typically, 32 GB per shot. The data is recorded in Volts with the range typically set to +/-1 V. A typical segment of raw data is shown in Fig. 3a. Several high-frequency bursts of magnetic fluctuations are seen in this figure. As this magnetic diagnostic is unshielded in the machine hall, it is also susceptible to electrical noise and pickup. An example of such electrical pickup is demonstrated by the broadband data spike at 0.912 s in Fig. 3(a–c). The level of the amplified magnetic fluctuations varies from 0.1 V_{pp} to 2 V_{pp}. These low voltage magnetic fluctuations are on the order of μW, whereas the highest fluctuations correspond to mW. However, it should be noted that the diagnostic only samples a small volume of the plasma so the total signal generated by the plasma is much larger. The amplitude and spatial response of this diagnostic is currently uncalibrated.

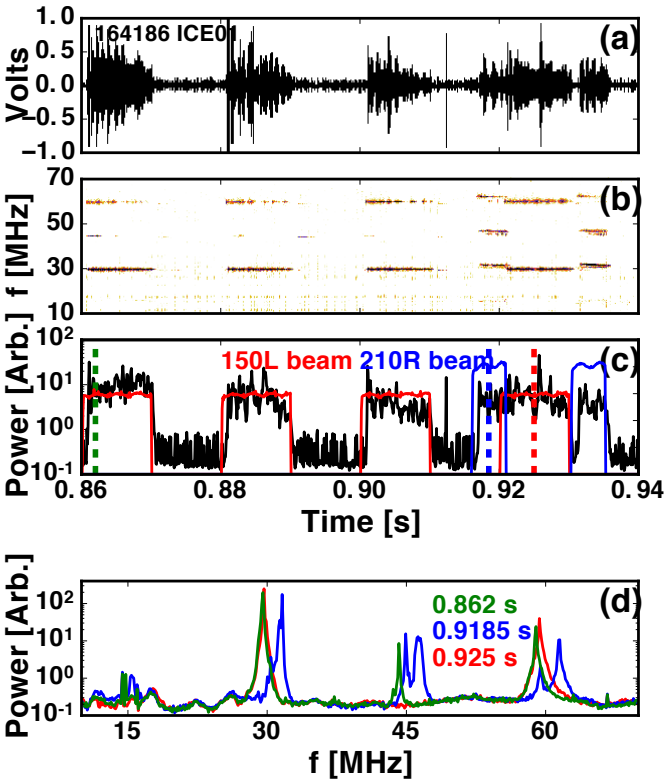

FIG. 3. Radio frequency magnetic fluctuations for DIII-D shot 164186 measured with the ICE diagnostic. (a) Amplified raw trace of fluctuations; (b) spectrogram; (c) average ICE power from 27.7–32.2 MHz (black) versus time with neutral beam heating from 150L beam (red) and 210R beam (blue); (d) ICE power at 0.862 s (green), 0.925 s (red), and 0.918 s (blue) with 2 ms averaging. These times are illustrated in (c) as dashed vertical lines.

III. ANALYSIS AND INITIAL RESULTS

The data analysis for the ICE diagnostic is conducted within the OMFIT integrated modeling framework[24]. A dedicated OMFIT `ICE` module was developed and used to perform detailed analysis of over 50 DIII-D discharges. The OMFIT `ICE` module provides a front end for data fetching, signal processing, and data visualization for the ICE diagnostic. The high sampling rate of the ICE signals result in large data sets, which required developing routines that were carefully crafted to avoid running out of memory while handling the data.

Specifically, the Windowed Fast Fourier transform (WFFT) analysis was carried out in such a way to always operate on only a single 80 ms data segment at a time ($\sim 2^{24}$ data points). Only the data segments that fall within a range of times selected by the user are analyzed. A typical WFFT analysis uses 2^{14} data points (corresponding to a $\sim$80 μs slice), weighted by a Hann window function in order to reduce the high-frequency side lobe contributions. The transformed slices from each of the 80 ms segments are usually downsampled by 10×, to preserve computer memory, and then joined together to form the final spectrogram. The resulting spectrograms are then stored within the OMFIT `ICE` module for further post-processing. The raw data is not typically stored within OMFIT after transforming the data to reduce computer memory usage.

The extremely large number of data points is such that even plotting the raw data is a non-trivial task, which is occasionally performed for only a few segments of data. A simple down-sampling approach was first attempted but later discarded because important features in the signal might be missed. Hence, a dedicated plotting routine that bins the data then plots the maximum and minimum value in each of the bins was developed. As the time range or voltage range is changed in this plot, the bins are automatically recalculated and replotted. This plotting method was found to be over 100× faster than plotting all the data points, and capable of conveying the salient raw data information to the user.

An example of this data analysis approach is shown in Fig. 3. The raw data in Fig. 3(a) is Fourier transformed in Fig. 3(b). The frequency range has been decreased for clarity. High-frequency emission is observed at several frequencies in this figure, correlating with the raw magnetic fluctuations observed in Fig. 3(a). Typically, the ICE power at specific frequencies or times of data are analyzed as demonstrated in Fig. 3(c–d). The time variation of the averaged power of the signal from 27.2–

32.2 MHz is shown in Fig. 3(c) as well as the pulses of injected neutral beams. As shown here, these high-frequency magnetic fluctuations occur with the application of neutral beam injection. Three timeslices with 2 ms averaging times during this discharge are analyzed further in Fig. 3(d). The ICE power frequency spectrum differs for these times, due primarily to the different injected beams. The frequency spectra at 0.862 s and 0.925s are very similar due to the use of the same beam (150L); whereas at 0.9185 s with the injection of the 210R neutral beam, the frequency spectrum is shifted to slightly higher frequencies when compared to the other two time points. The ICE signal-to-noise ratio at a given time for any discharge can be improved by increasing this averaging time; typically 0.001 to 1 s averaging times are employed depending upon the signal strength and the noise level.

Using this diagnostic, three different types of energetic-particle-driven emission have been observed and are being characterized on DIII-D. The signal shown in Fig. 3 corresponds to ICE, which is the ICRF emission most often observed with this diagnostic. ICE is observed at harmonics of f_{ci}, with resulting frequencies ranging from 5–100 MHz. CAEs are occasionally observed on DIII-D with $f < f_{ci}$, corresponding to 2–10 MHz. Whistler waves are observed only in low density or disrupting plasmas at $f >> f_{ci}$, corresponding to 100-200 MHz. These three types of energetic-particle-driven emission will be described in greater detail in forthcoming publications, including Spong *et al.*[21]

Since ICE has been theoretically predicted[25,26] and experimentally observed[3,4,6,10,12–14,16] to occur at harmonics of f_{ci}, the radial location of the emission, assuming no or only a small Doppler shift, can be determined. The radial location of CAEs and whistler waves is not as easily determined, so this diagnostic primarily serves as a global indicator of excitation for them.

The location of ICE is determined by matching the magnetic field to a particular ICE frequency by using the EFIT equilibrium reconstruction code[27]. In Fig. 3(d) at 0.862 s, three frequency peaks are clearly observed. These peaks are at 29.56, 44.22, and 58.88 MHz, with spacing of 14.66 MHz. The plasmas shown in this paper are deuterium plasmas with deuterium neutral beam heating. Thus, these peaks correspond to the second, third and fourth harmonics of the deuterium cyclotron frequency $f_{cD} = 14.66$ MHz. The dominance of the second harmonic and weakness of the fundamental frequency is not atypical for DIII-D plasmas and has been observed elsewhere[28]. EFIT, constrained via only the magnetic diagnostics, was used to calculate the magnetic field at this discharge time in Fig. 4. The various magnetic field components from EFIT are shown at the midplane in Fig. 4(a). The total magnetic field B_{TOT} is the square root of the sum of the squares of the toroidal B_T, radial B_R and vertical B_Z magnetic fields. As demonstrated in this figure, the toroidal field dominates the other fields and for the most part determines the total magnetic field on DIII-D. In Fig. 4(b), B_{TOT} is shown for three vertical locations, highlighting the near-invariance of B_{TOT} with vertical position. These figures illustrate that it is possible to determine the radial position of ICE

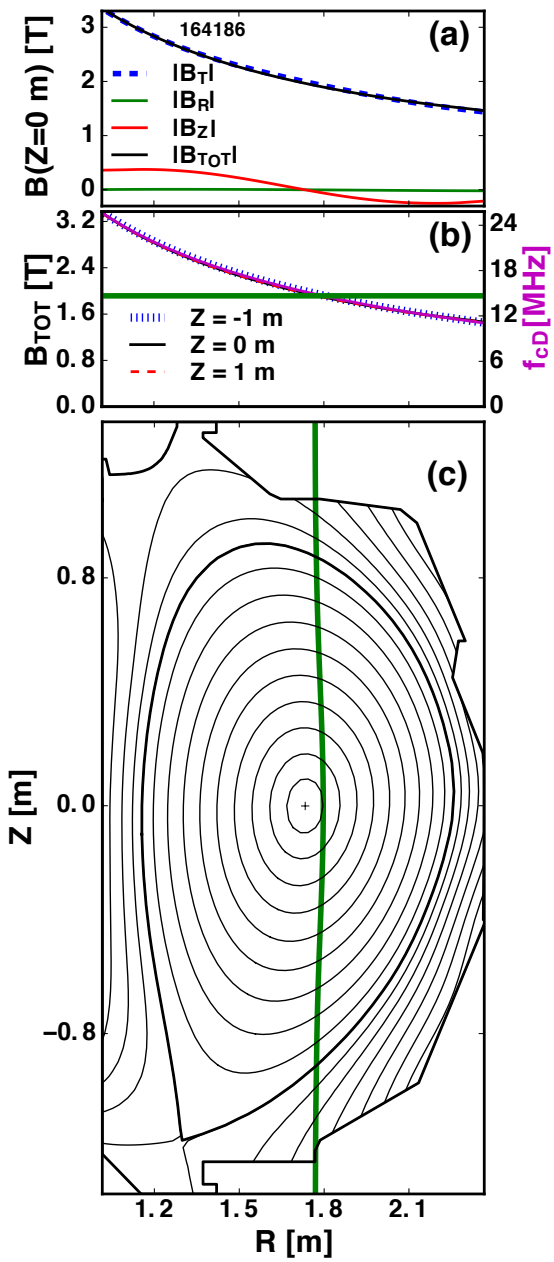

FIG. 4. Location of ICE in shot 164186 at 0.862 s. (a) Magnitude of the magnetic field components from EFIT: toroidal B_T, radial B_R and vertical B_Z, and total B_{TOT} magnetic fields at the midplane; (b) Total magnitude of the magnetic field at three Z locations from EFIT, f_{cD} on the midplane, and contour at 14.66 MHz (green) representing the fundamental ICE frequency; (c) EFIT equilibrium reconstruction at 0.862 s with green line indicating the ICE location.

but not the vertical position from its measured fundamental frequency. f_{cD} varies in this plasma from ∼25 MHz on the high-field-side plasma to ∼11 MHz on the low-field-side of the plasma. The toroidal field applied to DIII-D plasmas typically is in the range of 1–2 T on axis; in this plasma the field was ∼2 T. Hence f_{cD} is in the range of 5–26 MHz in DIII-D plasmas. Typically, only one harmonic (generally the fundamental) is present within the plasma, aiding in the identification of the radial location of the ICE excitation. Finally, in Fig. 4(c),

the EFIT equilibrium reconstruction is shown for this discharge time, as well as a contour representing the radial location of f_{cD} =14.66 MHz . Thus, in this plasma at this time, ICE is likely emitted from R≈1.8 m. Emission of ICE from this region of the plasma is routinely observed in many DIII-D plasmas.

In summary, this version of the ICE diagnostic was established in 2015 and expanded in 2017 to document ICRF emission driven by energetic particles. Several possible upgrades that could be done in the future to improve and expand this high-frequency diagnostic, include: improving the DC break frequency response and bandwidth, reduction of noise and electrical pickup, amplitude calibration, digitization at higher frequency, and expansion of the diagnostic by replacing the high-field-side centerstack loops described in Ikezi *et al.*[29] that are no longer operable.

ACKNOWLEDGMENTS

The authors thank A. Nagy for his support of this diagnostic. The authors also thank C. Chrobak for the image of this diagnostic system. This work was supported by the US Department of Energy under DE-FC02-04ER54698. The data shown in this paper can be obtained in digital format by following the links at `https://fusion.gat.com/global/D3D_DMP`.

[1]ITER Physics Expert Group on Energetic Particles and Heating and Current Drive and ITER Physics Basis Editors, Nuclear Fusion **39**, 2471 (1999).

[2]A. J. H. Donné, A. E. Costley, R. Barnsley, H. Bindslev, R. Boivin, G. Conway, R. Fisher, R. Giannella, H. Hartfuss, M. G. von Hellermann, E. Hodgson, L. C. Ingesson, K. Itami, D. Johnson, Y. Kawano, T. Kondoh, A. Krasilnikov, Y. Kusama, A. Litnovsky, P. Lotte, P. Nielsen, T. Nishitani, F. Orsitto, B. Peterson, G. Razdobarin, J. Sanchez, M. Sasao, T. Sugie, G. Vayakis, V. Voitsenya, K. Vukolov, C. Walker, K. Young, and the ITPA Topical Group on Diagnostics, Nuclear Fusion **47**, S337 (2007).

[3]R. D'Inca, K. McClements, D. C. Pace, P. Jacquet, S. E. Sharapov, T. Akiyama, G. S. Yun, R. Dumont, ASDEX Upgrade Team, JET contributors, and MST1 Teams, in *Proceedings of the 26th IAEA Fusion Energy Conference* (Kyoto, Japan, 2016).

[4]K. McClements, R. D'Inca, R. Dendy, L. Carbajal, S. Chapman, J. Cook, R. Harvey, W. Heidbrink, and S. Pinches, Nuclear Fusion **55**, 043013 (2015).

[5]J. Luxon, Nuclear Fusion **42**, 614 (2002).

[6]D. C. Pace, W. W. Heidbrink, M. A. Van Zeeland, and Y. Zhu, in *Proc. 43rd EPS Conf. on Plasma Physics* (Leuven, Belgium, 2016).

[7]H. Duong, W. Heidbrink, E. Strait, T. Petrie, R. Lee, R. Moyer, and J. Watkins, Nuclear Fusion **33**, 749 (1993).

[8]A. Axley and R. I. Pinsker, Bull. Am. Phys. Soc. **54**, 160 (2009).

[9]W. W. Heidbrink, M. E. Austin, R. K. Fisher, M. García-Muñoz, G. Matsunaga, G. R. McKee, R. A. Moyer, C. M. Muscatello, M. Okabayashi, D. C. Pace, K. Shinohara, W. M. Solomon, E. J. Strait, M. A. Van Zeeland, and Y. B. Zhu, Plasma Physics and Controlled Fusion **53**, 085028 (2011).

[10]TFR Equipe, Nuclear Fusion **18**, 1271 (1978).

[11]S. Cauffman, R. Majeski, K. G. McClements, and R. O. Dendy, Nuclear Fusion **35**, 1597 (1995).

[12]G. Cottrell, V. P. Bhatnagar, O. D. Costa, R. O. Dendy, J. Jacquinot, K. G. McClements, D. C. McCune, M. F. F. Nave, P. Smeulders, and D. F. H. Start, Nuclear Fusion **33**, 1365 (1993).

[13]R. D'Inca, M. García-Muñoz, G. Tardini, J.-M. Noterdaeme, and ASDEX Upgrade Team, in *Proc. 38th EPS Conf. on Plasma Physics* (Strasbourg, France, 2011).

[14]M. Ichimura, H. Higaki, S. Kakimoto, Y. Yamaguchi, K. Nemoto, M. Katano, M. Ishikawa, S. Moriyama, and T. Suzuki, Nuclear Fusion **48**, 035012 (2008).

[15]S. G. Thatipamula, G. S. Yun, J. Leem, H. K. Park, K. W. Kim, T. Akiyama, and S. G. Lee, Plasma Physics and Controlled Fusion **58**, 065003 (2016).

[16]K. Saito, R. Kumazawa, T. Seki, H. Kasahara, G. Nomura, F. Shimpo, H. Igami, M. Isobe, K. Ogawa, K. Toi, M. Osakabe, M. Nishiura, T. Watanabe, S. Yamamoto, M. Ichimura, T. Mutoh, and L. E. Group, Plasma Science and Technology **15**, 209 (2013).

[17]W. W. Heidbrink, E. D. Fredrickson, N. N. Gorelenkov, T. L. Rhodes, and M. A. Van Zeeland, Nuclear Fusion **46**, 324 (2006).

[18]E. D. Fredrickson, N. Gorelenkov, C. Z. Cheng, R. Bell, D. Darrow, D. Johnson, S. Kaye, B. LeBlanc, J. Menard, S. Kubota, and W. Peebles, Phys. Rev. Lett. **87**, 145001 (2001).

[19]L. C. Appel, T. Fülöp, M. J. Hole, H. M. Smith, S. D. Pinches, R. G. L. Vann, and The MAST Team, Plasma Physics and Controlled Fusion **50**, 115011 (2008).

[20]D. Stutman, L. Delgado-Aparicio, N. Gorelenkov, M. Finkenthal, E. Fredrickson, S. Kaye, E. Mazzucato, and K. Tritz, Phys. Rev. Lett. **102**, 115002 (2009).

[21]D. Spong, W. W. H. C. P.-S. X. D. Du, K. E. Thome, M. A. Van Zeeland, C. Collins, A. Lvovskiy, R. A. Moyer, D. P. Brennan, C. Liu, E. F. Jaeger, and C. Lau, accepted in Phys. Rev. Lett. (2018).

[22]G. Watson and W. W. Heidbrink, Review of Scientific Instruments **74**, 1605 (2003), https://doi.org/10.1063/1.1527222.

[23]G. W. Watson, W. W. Heidbrink, K. H. Burrell, and G. J. Kramer, Plasma Physics and Controlled Fusion **46**, 471 (2004).

[24]O. Meneghini, S. Smith, L. Lao, O. Izacard, Q. Ren, J. Park, J. Candy, Z. Wang, C. Luna, V. Izzo, B. Grierson, P. Snyder, C. Holland, J. Penna, G. Lu, P. Raum, A. McCubbin, D. Orlov, E. Belli, N. Ferraro, R. Prater, T. Osborne, A. Turnbull, and G. Staebler, Nuclear Fusion **55**, 083008 (2015).

[25]R. O. Dendy, K. G. McClements, C. N. LashmoreDavies, R. Majeski, and S. Cauffman, Physics of Plasmas **1**, 3407 (1994), https://doi.org/10.1063/1.870489.

[26]N. N. Gorelenkov, New Journal of Physics **18**, 105010 (2016).

[27]L. Lao, H. S. John, R. Stambaugh, A. Kellman, and W. Pfeiffer, Nuclear Fusion **25**, 1611 (1985).

[28]L. Carbajal, R. O. Dendy, S. C. Chapman, and J. W. S. Cook, Physics of Plasmas **21**, 012106 (2014), https://doi.org/10.1063/1.4861866.

[29]H. Ikezi, R. I. Pinsker, S. C. Chiu, and J. S. DeGrassie, Physics of Plasmas **3**, 2306 (1996), https://doi.org/10.1063/1.871913.